Stereolithography 3D printing of microgroove master moulds for topography-induced nerve guidance conduits

Yue, Hexin; Liu, Xuzhao; Hou, Kejian; Vyas, Cian; Bartolo, Paulo

2024

https://hdl.handle.net/10356/180503

https://doi.org/10.36922/ijb.2725

RESEARCH ARTICLE

Stereolithography 3D printing of microgroove master moulds for topography-induced nerve guidance conduits

Hexin Yue[1], Xuzhao Liu[1], Kejian Hou[1], Cian Vyas[1,2*], and Paulo Bartolo[1,2*]

[1]School of Mechanical, Aerospace and Civil Engineering, University of Manchester, Manchester, United Kingdom

[2]Singapore Centre for 3D Printing, School of Mechanical and Aerospace Engineering, Nanyang Technological University, Singapore

*Corresponding authors:
Cian Vyas
(cian.vyas@ntu.edu.sg)

Paulo Bartolo
(paulojorge.dasilvabartolo@
manchester.ac.uk)

Abstract

Patients who have peripheral nerve damage from trauma or disease may suffer lifelong disability. Current interventions such as nerve allografts are inadequate due to limited availability of tissue and donor-site morbidity. Commercial nerve guidance conduits are used to bridge the damaged nerve gap and restore function. Typically, however, they lack cell-instructive guidance cues to promote directed regeneration. Tissue-engineered nerve guidance conduits that utilise micro- and nano-topographical architectures have been demonstrated to direct cell behaviour and contact guidance. This study uses projection micro-stereolithography-based three-dimensional (3D) printing to fabricate microgrooved (10–30 μm) master moulds to produce polydimethylsiloxane (PDMS) moulds and solvent cast polycaprolactone and polylactic acid films. The polymer microgrooves were successfully fabricated and were able to be formed into tubular nerve guidance conduits. The surface morphology, roughness, wettability, and thermal properties of the films were characterised. The microgroove topography improved proliferation and induced alignment of SH-SY5Y cells. This facile 3D printing approach is promising for the fabrication of nerve guidance conduits with topographical guidance cues as it obviates the need for using photolithographic techniques. Thus, this approach provides an alternative that is simpler, faster, cheaper, and offers greater design freedom.

Keywords: Bioprinting; Microgroove; Moulds; Nerve guidance conduit; Peripheral nerve repair; Stereolithography

1. Introduction

The peripheral nervous system (PNS) connects the central nervous system to the entire body, with its principal responsibilities encompassing the processing of incoming neural information, modulation of sensory perception, coordination of motor activities, and the preservation of homeostasis. Peripheral nerve injury (PNI) is a frequent occurrence, typically arising from trauma, and results in a complicated recovery process related to the specific gap size and the slow regeneration speed. Globally, there are over 5 million new cases of PNI annually.[1] Spontaneous regeneration of nerves is feasible for small gaps

measuring a few millimetres.[2] However, for larger nerve gaps, a regenerative rate of 1–3 mm per day is imperative for axons to reach the distal motor endplate, frequently leading to partial functional recovery.[3]

Current clinical interventions for PNI predominantly involve suturing and autologous transplantation.[4,5] The precision required in nerve suturing may result in excessive tension, and autologous transplantation encounters limitations due to donor tissue constraints and structural disparities between donor and recipient nerves. Clinically, up to 33% of PNI cases exhibit incomplete recovery and adverse outcomes, including chronic pain, compromised or partially restored motor and sensory function, and muscular atrophy and weakness.[6]

Peripheral nerves have a multi-fascicle structure with axons orientated in the same direction in each fascicle.[7] When peripheral nerves are injured, the nerve cells align longitudinally in the endoneurium, generating Büngner bands to direct the axons. Notably, when the PNI gap exceeds 10 mm, grafting interventions become imperative to bridge the proximal and distal nerve stumps, thereby fostering the requisite environment for regeneration.[8] The efficiency of nerve regeneration is enhanced when cell arrangement and axonal growth are directed.[9]

Commercially available nerve guidance conduits (NGCs) typically adopt a single-channel configuration.[10] They are usually restricted to short injury gaps (<20 mm) due to the absence of specific guidance cues.[11,12] Furthermore, single-channel nerve conduits are susceptible to collapse, impeding nerve growth, inadequately mimicking fascicle structures, and exhibiting suboptimal performance in guiding axonal growth.[13] Microchannel NGCs, whilst capable of directing cell alignment and promoting regenerating axons to aggregate in natural bundles, also present challenges such as potential insufficient nutrient supply to the regenerating tissue within the lumen.[5,14]

Tissue-engineered NGCs have been explored as potential alternatives to autografts.[5,14] NGCs are envisioned to serve as bridging devices capable of directing axonal growth and overcoming the impediments associated with traditional interventions. Various types of NGCs, including hydrogel fillers,[15] fibrous fillers,[16] and patterned scaffolds,[17] have been developed to create optimal intraluminal matrices for guiding neurite outgrowth. Specific guidance cues to direct regenerating axons to specific locations are essential.[18] Failure to provide guiding cues can result in dislocations, neuroma formation, and misconnections as regenerated axons lose their growth orientation.[19] Physical contact guidance cues, such as channels, aligned fibres, and grooves, significantly influence neural cell behaviour and axon pathfinding.[12] The design of topographical cues

in NGCs to guide this directional growth has been shown to impact the morphology, adhesion, and proliferation of nerve cells. Topographical cues such as dots, pits, pillars, and grooves at the nano- and micro-scale can modulate cell behaviour, including cell morphology, alignment, proliferation, differentiation, and migration.[20,21]

Microgroove topographies have been explored as nerve guidance cues with the specific structure (e.g., shape, groove depth, groove width and spacing) influencing cell response.[22,23] Various synthetic NGCs based on biodegradable polyesters with microgroove architectures have shown promising potential including poly(ε-caprolactone) (PCL), poly-l-lactic acid (PLA), and poly(lactide-coglycolide).[24,25] Typically, the microgroove dimensions are between 5 μm and 60 μm as this range enables contact guidance for neuronal cell types.[9,26-36] For example, Béduer et al.[27] observed that microgroove-patterned polydimethylsiloxane (PDMS) substrates with small microgroove widths (5–10 μm) improved axonal alignment and reduced branching in human neural stem cells but delayed neurite development and differentiation compared to larger groove widths (20–60 μm). Hsu et al.[26] fabricated chitosan and PLA microgroove conduits (20/20/3 μm) that improved Schwann and glial cell orientation and neurotrophic factor expression *in vitro* and enhanced peripheral nerve regeneration *in vivo*. A conductive polydopamine-coated poly(L-lactide-caprolactone)/graphene (PLCL/GN) composite NGC with 20 μm microgrooves was shown to promote directional migration, cell adhesion, elongation, myelin sheath growth, more rapid neuron regeneration, and functional recovery *in vivo*.[28] Apart from microgroove dimensions, the morphology of the microgroove has been demonstrated to be important by Mobasseri et al.,[29,30] with V- and sloped-shaped grooves showing improved cell alignment, as compared with square grooves.

However, the studies that explored microgroove NGCs mostly utilised photolithography to fabricate the master mould. Photolithography and soft microlithography techniques allow the fabrication of highly detailed nano- and micro-scale-patterned moulds.[37] These are transferred to the biomaterial substrate through an intermediate (e.g., PDMS mould or stamp) followed by solvent casting or thermal pressing.[14,27,30,31,38] However, photolithography is expensive and time-consuming, as well as requires stringent clean room facilities and entails complex processing steps. Soft lithography can be performed generally outside a clean room with a wider range of materials but still relies on the generation of a master mould via photolithography. Thus, this limits research accessibility, design freedom, and inability to rapidly prototype different configurations.

The resolution and capability of three-dimensional (3D) printing technology is improving, offering the benefits of design flexibility, precise geometric control, and wide variety of applicable materials. Subsequently, 3D printing has extensively been explored in biomedical applications, although the resolution of extrusion and inkjet-based machines is limited for fabricating microgroove architectures. Light-based vat photopolymerisation, such as stereolithography (SL), offers high resolution and has been utilised to fabricate NGCs with single- and multi-channel architectures.[39-42] For example, Pateman et al.[42] developed a single-channel NGC that exhibited an axially aligned microtopography due to the pixelation effect in digital light processing (DLP). However, a photocurable biomaterial is required for direct NGC fabrication, thus restricting the materials applicable.

SL has been used as an alternative to photolithography in the fabrication of master moulds for microfluidics.[43] Moulds can be rapidly fabricated and iterated at a lower cost than conventional photolithography. This makes them suitable for soft lithography and casting of PDMS, a polymer used for intermediate templates and prototyping microfluidic devices due to the relatively chemical inertness, biocompatibility, low cost, and transparency in ultraviolet-visible spectrum.[44] However, this approach has not yet been explored for the specific design and fabrication of cell-instructive microgroove topographies in NGCs.

This study explores the replacement of photolithography with SL for the fabrication of master moulds for the development of microgroove NGCs using soft lithography. Considering dimensions commonly employed in the literature to support contact guidance for neuronal cells, four different microgroove master mould architectures were fabricated: 10/10/10 µm, 20/20/10 µm, 25/25/10 µm, and 30/30/10 µm (width/spacing/depth). The 3D-printed master mould was used to fabricate a PDMS mould to enable casting of PCL and PCL/PLA thin films. The morphology, roughness, mechanical, wettability, and thermal properties were characterised, and SH-SY5Y cells were seeded to evaluate morphology and proliferation. This approach highlights the capability of high-resolution 3D printing to compete with photolithography in specific applications. Furthermore, this study provides understanding of appropriate microgroove dimensions to promote cell alignment for NGC applications.

2. Material and methods

2.1. Materials
PCL (Mn 80,000 g/mol), PLA (Mn 30,000 g/mol), SYLGARD™ 184 poly(dimethylsiloxane) (PDMS), foetal bovine serum (FBS), trypsin-EDTA, penicillin–

streptomycin, glutamine, all-trans-retinoic acid (ATRA), paraformaldehyde (PFA), and Triton X-100 were purchased from Sigma-Aldrich (UK). Dichloromethane (CH_2Cl_2), Ethanol, Dulbecco's phosphate-buffered saline (PBS), DMEM/F-12, AlamarBlue™ Cell Viability Reagent, LIVE/DEAD Viability/Cytotoxicity Assay Kit, Alexa Fluor® 488 Phalloidin, and DAPI (4′,6-diamidino-2-phenylindole) were purchased from Thermo Fisher Scientific (UK). SH-SY5Y (human neuroblastoma cell line CRL-2266) was purchased from ATCC (USA).

2.2. Design and 3D printing of master moulds
The master moulds were designed by computer-aided design (CAD) software (Siemens NX, Germany) with dimensions of 12.5 × 12.5 × 1 mm (*xyz*). Four different surface topographies were considered with microgroove dimensions of 10/10/10 µm, 20/20/10 µm, 25/25/10 µm, and 30/30/10 µm (width, spacing, and depth) (Figure 1a). A projection micro-stereolithography (PµSL) 3D printer (MicroArch™ S130, Boston Micro Fabrication, USA) with *x–y* resolution of 2 µm, layer thickness of 5–20 µm, and build volume of 50 × 50 × 10 mm (*xyz*) was used to fabricate the master moulds using the HTL photopolymer resin (Boston Micro Fabrication, USA). The 3D-printed moulds were examined using an upright digital microscope (VHX-5000, Keyence, Japan).

2.3. Fabrication of PDMS moulds and microgroove films
The fabrication of microgroove topographies on polymer films involves multiple steps (Figure 1b). Residual photoinitiators and unreacted oligomers may be left behind in the 3D-printed master mould, inhibiting PDMS curing.[45] To minimise inhibition, the 3D-printed master moulds were immersed in 95% ethanol for 24 h in a sealed container and placed on a shaker. The ethanol was removed and refreshed, sealed, and shaken for another 24 h. The moulds were then rinsed with water and air-dried for 1 h at room temperature.

The PDMS was mixed at a 10:1 (wt./wt.) ratio of prepolymer to curing agent, degassed under vacuum to remove air bubbles, and poured onto the 3D-printed master moulds to achieve a thickness of ~10 mm. The moulds were placed at the bottom of the PDMS prepolymer to guarantee the same solution volume can be casted onto the PDMS moulds. The PDMS was cured overnight (12–16 h) in a dry oven at 65°C. The moulds were removed to release the cured PDMS mould. No releasing agents were required for the release of PDMS replicas.

A 1, 3, and 5% wt./vol PCL and blend of PCL/PLA (4:1) solution in dichloromethane (DCM) was prepared and casted onto the microgroove PDMS moulds
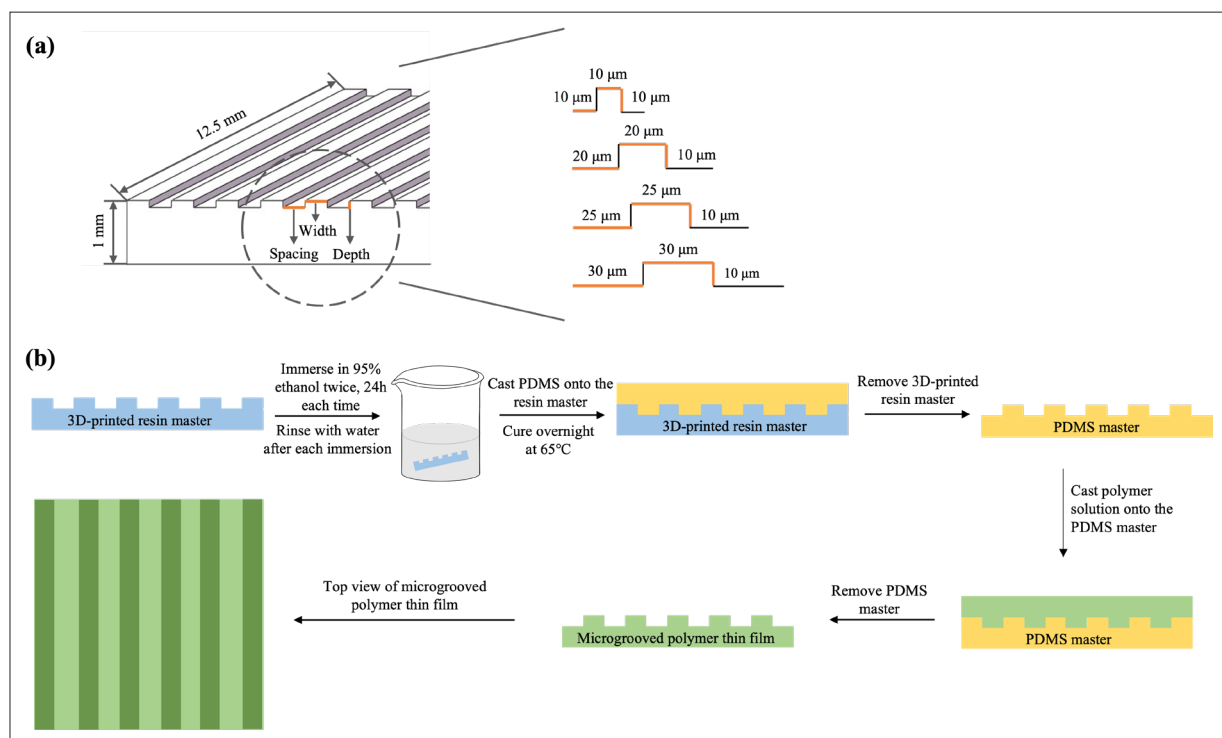
Figure 1. (a) Design specification of 3D-printed moulds with designs of 10/10/10 μm, 20/20/10 μm, 25/25/10 μm, and 30/30/10 μm; and (b) the procedures for preparation of the microgrooved PCL or PCL/PLA substrates.

([Figure 1b](#)). The solutions were left to evaporate in a fume cabinet for 1 h, and the casted films were removed. Microgroove samples consisting of the designs, flat (no microgrooves), 10/10/10 μm, 20/20/10 μm, 25/25/10 μm, and 30/30/10 μm, are referred to as PCL-F, PCL-10, PCL-20, PCL-25, and PCL-30 or PCL/PLA-F, PCL/PLA-10, PCL/PLA-20, PCL/PLA-25, and PCL/PLA-30, respectively. Different layer thicknesses (~10, 20, or 30 μm) of thin films were produced by using different volumes of polymer solution, and the thickness of casted films was inspected with a digital calliper. Except for mechanical testing, 20 μm thick samples were utilised throughout the study.

2.4. Morphology and roughness of moulds and microgroove films

The 3D-printed moulds, PDMS moulds, and casted microgroove films were assessed using an upright digital light microscope (VHX-5000, Keyence, Japan), a laser scanning confocal microscope (LSCM; VK-X250, Keyence, Osaka, Japan), a scanning electron microscope (SEM; Zeiss Sigma VP, Carl Zeiss, USA), and an atomic force microscope (AFM; Multimode 8-HR, Bruker, Germany).

The LSCM with 120 nm lateral resolution using a 408 nm violet laser and a 16-bit photomultiplier to receive the laser light was utilised to analyse the surface topography (scan area: 95 × 71 μm and 50× magnification). The roughness of the upper groove surface (400×) was assessed with a scan area of 10 × 7 μm (20, 25, and 30 μm microgrooves) and 6 × 5 μm (10 μm microgroove). Images were post-processed using Gwyddion software.

The casted microgroove thin films for SEM were sputter-coated (Q150R S, Quorum Technologies, UK) with gold/palladium (80/20) to obtain ~6 nm thick coating. Images from the top surface of the microgroove thin film were captured and analysed using ImageJ software.[46]

The surface roughness of the thin films was analysed through AFM equipped with a ScanAsyst-Air probe (shape: pyramid; height: 10 μm; radius: <10 nm) in Peak Force tapping mode. The topographic profiles refer to scan areas of 0.5 × 0.5 μm with a resolution of 512 × 512 pixels. The image processing and roughness values measurement were performed by Gwyddion software.

2.5. Thermal evaluation

Thermogravimetric analysis (TGA) of the PCL, PLA, and PCL/PLA samples (mass ~10 mg) was performed using TA Instruments Q50 (TA Instruments, New Castle, USA). The test was carried out in an air atmosphere between 25 and 600°C with a heating rate of 10°C/min.

The differential scanning calorimetry (DSC) test, which analyses thermal behaviour and crystallisation of samples, was performed using TA Instruments Q-100 (TA Instruments, New Castle, USA) from 0 to 200°C at a heating rate of 10°C/min in a nitrogen atmosphere. The degree of crystallinity (X_c) and melting point (T_m) of PCL and PLA were determined. X_c was calculated using Equation I:

$$X_c \ (\%) = \Delta H_m / (f \times \Delta H_0) \times 100 \qquad \text{(I)}$$

where ΔH_m is the specific melting enthalpy of the sample, f is the weight percentage of PCL or PLA, and ΔH_0 is the melting enthalpy of completely crystalline polymer (132 J/g for PCL, 93.7 J/g for PLA).[47]

2.6. Tensile mechanical assessment

Tensile tests were conducted with the Instron 3344 (Instron, USA) and integrated software (Bluehill Universal, Instron, USA). The samples ($n = 5$), each measuring 1.5 mm and 10 mm, for width and length, respectively, were prepared. A crosshead speed of 1 mm/min, 6 mm grip distance, and a 10 N load cell were used with the force applied in parallel to the direction of the grooves. The samples were prepared with different thickness (10, 20, or 30 μm), different solvent concentration (1, 3, or 5 wt%), and different groove morphologies. The maximum tensile strength, the strain at breaking, and the Young's modulus were analysed using Origin software (OriginLab, USA).

2.7. Surface wettability

The wettability of the microgroove films was assessed by water contact angle (WCA) measurement. The microgroove thin films with different groove sizes, different materials, and different solvent concentrations were prepared for the WCA to examine the hydrophilicity. The wetting behaviour of the films ($n = 5$) was evaluated using a DSA100B (KRÜSS, Germany) with an image taken at 0 s and 60 s after droplet formation on the sample surface (static sessile drop). The contact angle was automatically calculated by Attention Theta software (Biolin Scientific, Sweden) through the sessile drop and drop profile fitting method.

2.8. *In vitro* cell culture

The SH-SY5Y neuroblastoma cell line (ATCC® CRL-2266) is a well-established *in vitro* model for neuronal differentiation and neurotoxicity.[48] SH-SY5Y cells were cultured in T75 cell culture flasks (Sigma-Aldrich, UK) with DMEM/F-12 (1:1, v:v) medium supplemented with 10% foetal bovine serum (FBS), 1% penicillin/streptomycin, and 1% glutamine, in an incubator at 37°C and 5% CO_2. The growth medium was changed every 3 days. Cells were sub-cultured after reaching 80–90% confluence by rinsing with PBS, trypsinising (0.25% Trypsin-EDTA), and neutralising with fresh media.

The microgroove films (3 wt% concentration and 20 μm thickness) were fixed in CellCrown™ inserts (Sigma-Aldrich, UK) within 48-well plates to prevent them from floating, sterilised with ethanol for 4 h, and washed twice with PBS. Cells were counted (Cellometer Auto 1000, Nexcelom Bioscience, USA), and films were seeded with 1.9×10^4 cells in 0.1 mL of cell culture medium specifically on the surface. After incubating for 30 min to allow the cells to attach, 0.4 mL of cell culture medium was added. The media was refreshed every 3 days.

2.9. Cell viability, proliferation, and morphology

The Alamar Blue assay was used to monitor cell metabolic activity, which serves as an indicator of cell viability and proliferation. Following the manufacturer's instructions, briefly, 50 μL of Alamar Blue solution was added to each well and incubated for 4 h at 1, 3, 5, and 7 days after cell seeding, and 150 μL of the solution was transferred to 96-well plate ($n = 5$). The fluorescence (ex 530 nm/em 590 nm) was measured by a microplate reader (Synergy HT, BioTec, USA). The well plate was changed every time after Alamar Blue assay.

Cell viability was observed on day 7 using a live/dead kit and following the manufacturer's instructions. Calcein-AM (green) and ethidium homodimer-1 (EthD-1) (red) were used to fluorescently label live and dead cells, respectively. Samples ($n = 3$) were washed three times with PBS before staining in a calcein-AM (1/2000 dilution) and EthD-1 (1/500 dilution) PBS solution and incubated for 20 min prior to imaging with a confocal microscope (Lecia SP-8 Lightning, Lecia Microsystems, Germany). A minimum of three images per sample and a minimum of 180 cells in total were used to calculate the percentage viability.

Cell morphology was observed on day 7. The samples ($n = 3$) were rinsed twice with PBS (37°C), fixed with 4% PFA for 15 min, washed with PBS three times, permeabilised with 0.1% Triton X-100 for 15 min at room temperature, and washed with PBS three times. A 5% FBS solution was then added to block non-specific binding, and the samples were incubated for 1 h and washed once with PBS. Alexa Fluor® 488 Phalloidin (1:400) in 1% FBS solution was added to each sample and incubated for 45 min at room temperature and protected from light. The samples were rinsed in PBS, and DAPI (1:1000) was added and incubated for 10 min at room temperature in the dark. The samples were washed twice with PBS and stored at 4°C prior to imaging. Cell morphology was visualised with confocal microscope (Leica SP8 Lightning, Leica Microsystems, Germany), and cell orientation was quantitatively analysed by ImageJ software.[46]

2.10. Statistical analysis

Statistical analysis, specifically one-way analysis of variance (ANOVA) with Tukey test, was carried out using Origin software (OriginLab, USA). The data are expressed as the mean ± standard deviation. The significance levels were set at $*P < 0.05$, $**P < 0.01$, and $***P < 0.001$ when comparing PCL and PCL/PLA with the same groove parameters.

3. Results and discussion

3.1. Morphology of moulds and microgroove films

Light microscopy and SEM were used to evaluate the suitability of 3D printing to fabricate micropatterned master moulds for the casting of PDMS moulds and subsequent solvent casting of microgroove substrates (Figure 2). The microgroove dimensions (width, spacing, and depth) of the master moulds and corresponding PDMS moulds and microgroove films are depicted in Table 1 and Table S1 (Supplementary File), based on the use of light microscopy and LSCM, respectively. The depth measurement accuracy is limited due to the limitations of light microscopy on these types of samples. Qualitative and quantitative observation of the 3D-printed master mould shows a highly ordered, smooth, and well-defined microgroove architecture that closely matches the design parameters (Figure 2a). Flat 3D-printed master mould and flat PDMS mould were fabricated as a control (Figure S1 in Supplementary File). These dimensions are closely transferred to the PDMS mould, and the microgrooves are clear and uniform, although surface deviations and imperfections are visible due to the casting process (Figure 2b). This evidently demonstrates the suitability of (PμSL) 3D printing for the fabrication of microscale master moulds for microgroove patterning.

The microgroove thin films consisting of PCL and PCL/PLA at different concentrations (1, 3, and 5 wt%) and dimensions were successfully fabricated using solvent casting (Figure 2c; Figure S2 in Supplementary File). As observed, the films present microgroove dimensions similar to the original design and the PDMS and 3D-printed moulds. The microgroove surfaces are smooth; however, there is a slight irregularity to the groove shape, which is not perfectly straight but is similar to other comparable microgroove PCL and PCL/PLA films.[29,49] Micro- and nanoscale pores are observed on the lower groove surface due to the rapid evaporation of DCM causing bubbling (Figure 2c, inset). Whilst the upper grooves have the presence of nano-fissures, potentially due to the greater thickness of material at this area and a slower evaporation rate during casting. To attenuate the rapid evaporation, a multi-solvent system can be explored to optimise the solvent casting process. The addition of PLA generally reduced the appearance of pores and fissures. Similarly,

lower polymer concentration solutions produced films with a smoother appearance (Figure S2 in Supplementary File).

To demonstrate the feasibility of this approach to fabricate NGCs, the film was rolled around a mandrel and sealed with an adhesive to form a tube with an inner diameter of 1.7 mm and length of 12.5 mm (Figure 2d-i and 2d-ii). SEM showed uniform microgroove structures on the inner wall of the NGC that act as topographical guidance pathways (Figure 2d-iii) and a clean seal (Figure 2d-iv). The tube was flexible and has dimensions suitable for NGC applications, warranting further study.

An alternative 3D printing system (M-50, CADworks3D, Canada) based on digital light processing (DLP) technology was similarly evaluated to determine the machine system specifications required to achieve dimensions suitable for NGCs (Figure S3 and Table S2 in Supplementary File). 3D-printed master moulds with microgroove dimensions of 100/100/50 μm, 150/150/50 μm, and 200/200/50 μm were achievable, but a smaller microgroove of 30/30/10 μm was not possible. Further study was discounted due to the inability of achieving a resolution suitable for NGCs.

The use of PμSL to fabricate microgroove topographies offers significant advantages and comparable results compared to conventional approaches such as photolithography, soft lithography, and electron beam lithography that have been utilised up till now. The lower production cost, shorter experimental time, ease of access, and greater design freedom can allow more complex 3D structures to be fabricated for use in casting rather than traditional planar substrates. However, the PDMS mould degrades with multiple exposures to the solvent. Thus, differences between batches are possible, and the PDMS mould should be replaced once noticeable deterioration in microgroove quality is observed.

3.2. Surface roughness

The surface roughness of the microgroove films with different concentrations was evaluated using AFM with a scan area of 0.5 μm² (Figure 3a). The mean roughness (Sa) values of the 3 wt% PCL, PLA, and PCL/PLA surface are 8.31 nm, 4.28 nm, and 4.20 nm, respectively. The addition of PLA reduces the surface roughness, agreeing with the SEM observations. The 1 wt% samples show consistently lower surface roughness than the 3 and 5 wt% films. There is a change in nanoscale features from a relatively homogenous and smooth appearance at 1 wt% to a more spherical and undulating surface at higher concentrations.

LSCM was used to map the 3D topographic surface of the 3D-printed master mould and microgroove films at
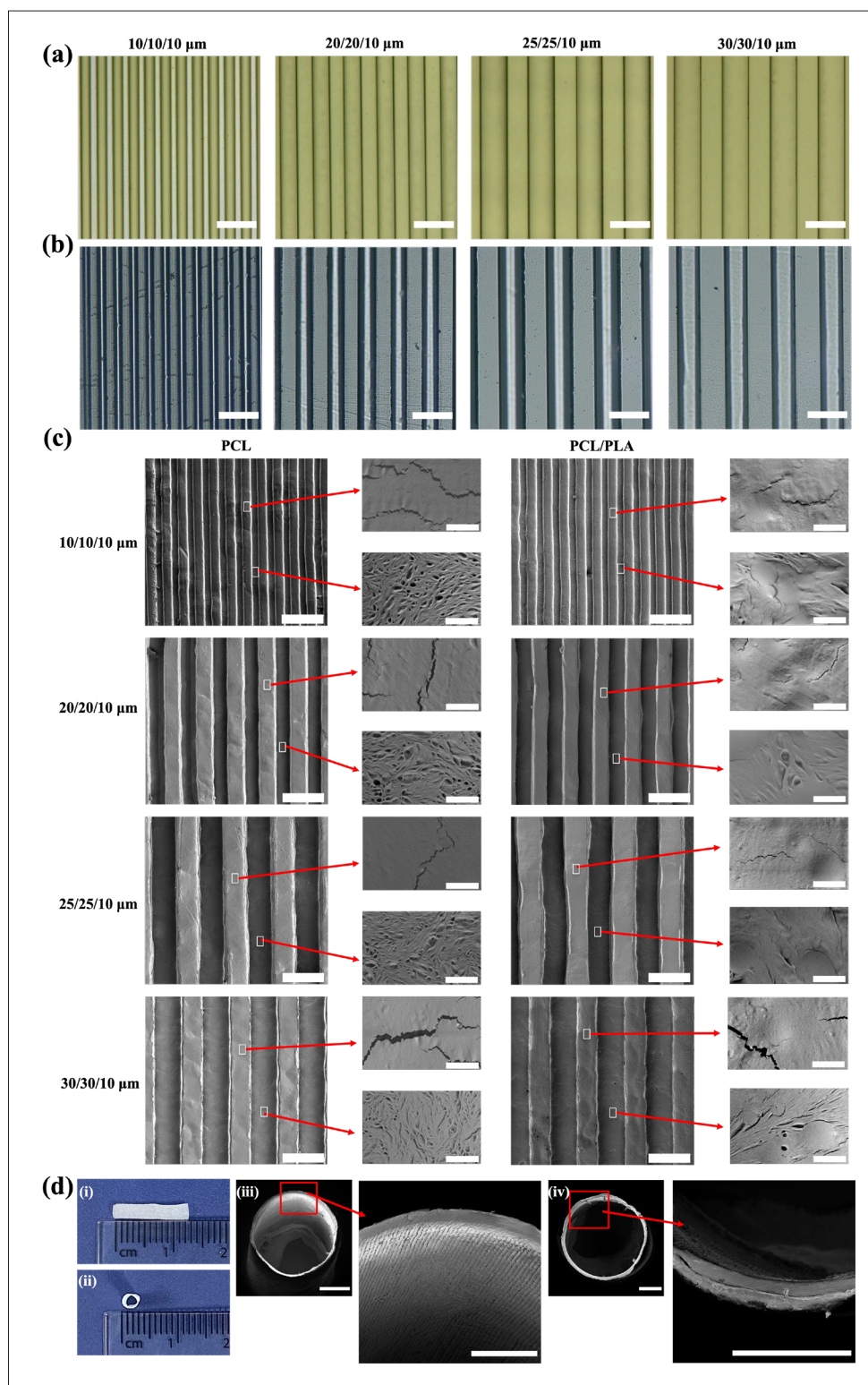
Figure 2. (a) Microscope images of 3D-printed moulds (scale bar: 50 µm) and (b) PDMS moulds (scale bar: 50 µm). (c) SEM images of the 3 wt% PCL and PCL/PLA thin films with different groove architectures: 10/10/10 µm, 20/20/10 µm, 25/25/10 µm, and 30/30/10 µm (scale bar: 50 µm; inset images scale bar: 1 µm). (d) Rolled and sealed PCL-10 NGC tube showing a photograph of (i) the side view, (ii) top view, and SEM image of (iii) inside the tube with microgroove topography and (iv) location of the film overlap and sealant (scale bar: 500 µm; low- and high-magnification images scale bar: 500 µm).

Table 1. Dimensions of the 3D-printed master moulds, PDMS moulds, and microgroove films, based on light microscopy

	Average width (µm)			Average spacing (µm)			Average depth (µm)		
	Master mould	PDMS mould	Casted film	Master mould	PDMS mould	Casted film	Master mould	PDMS mould	Casted film
PCL-10	10.44 ± 0.38	9.53 ± 0.56	11.74 ± 0.37	9.69 ± 0.75	10.35 ± 0.36	8.97 ± 0.56	10.38 ± 0.52	11.78 ± 0.67	12.47 ± 0.89
PCL-20	20.44 ± 0.73	19.28 ± 0.78	21.21 ± 1.03	19.4 ± 0.84	20.24 ± 0.56	18.56 ± 0.67	12.51 ± 0.87	12.96 ± 0.90	13.67 ± 0.66
PCL-25	25.52 ± 0.64	24.08 ± 0.81	26.39 ± 1.73	24.13 ± 0.85	25.47 ± 0.49	23.75 ± 0.86	14.15 ± 0.92	14.83 ± 0.75	15.91 ± 0.73
PCL-30	30.61 ± 0.67	28.68 ± 0.57	31.94 ± 1.21	28.85 ± 0.64	30.44 ± 0.66	27.28 ± 0.97	13.59 ± 0.63	13.87 ± 0.69	14.87 ± 0.79
PCL/PLA-10	/	/	11.41 ± 0.55	/	/	9.13 ± 0.63	/	/	12.38 ± 0.59
PCL/PLA-20	/	/	20.44 ± 0.23	/	/	18.87 ± 0.56	/	/	13.32 ± 0.61
PCL/PLA-25	/	/	26.30 ± 1.01	/	/	24.09 ± 0.78	/	/	15.34 ± 0.71
PCL/PLA-30	/	/	31.48 ± 1.27	/	/	27.85 ± 0.88	/	/	14.29 ± 0.76

The 3D-printed master moulds and PDMS moulds are the same for both PCL and PCL/PLA groups.

both large (95 × 71 µm) and small (10 × 7 µm) scan areas (Figure 3b). The PDMS moulds were not able to be assessed using LSCM due to the optical transparency. This revealed that the 3D-printed master moulds had significantly lower surface roughness (root mean square height area roughness, Sq: ~90.9 nm; arithmetical mean height area roughness, Sa: ~68.6 nm) than the microgrooved films (Sq: ~371.4 nm, Sa: ~248.1 nm) (Figure 3b-ii and 3b-iii). The PDMS moulds appear smooth, although further quantitative verification is required. The subsequent microgroove pattern transfers from the original 3D-printed master mould to the PDMS mould, and finally, the polymer film introduces a considerable amount of surface roughness.

The PCL films had an average mean surface roughness, Sa, of 331.83 nm, which was higher than PCL/PLA of 167.65 nm. The PCL microgroove films have a consistent surface roughness even with different microgroove sizes. However, the PCL/PLA-25 and 30 groove sizes (Sa: ~118.3 nm) showed a lower roughness than the PCL/PLA-10 and 20 (Sa: ~217 nm). A similar trend is observed for Sq. Surface measurements including skewness (Ssk), kurtosis (Sku), and maximum peak, pit depth, and height are shown in Table S3. All the moulds and microgroove films have an Ssk close to 0 and are generally positive, indicating a height distribution close to the mean surface plane with peaks. The Sku is predominately below 3, representing a lack of high peaks or deep valleys.

3.3. Thermal evaluation

DSC was used to assess the thermal and crystallisation properties of PCL, PLA, and the PCL/PLA blend with different concentrations (1, 3, and 5 wt%) (Figure 4 and Table 2). The T_m of PCL/PLA blend is consistently slightly lower than PCL and PLA at the same concentration, which can be seen clearly with the shift in the DSC curves (dotted lines). The ΔH_m for PCL and PLA are both

decreased after they are blended. TGA and derivative thermogravimetric analysis were additionally assessed to understand the thermal degradation behaviour (Figure S4 in Supplementary File).

The crystallinity data indicate that PCL is highly crystalline (X_c ~55%), whilst PLA has a considerably lower crystallinity (X_c ~25%). Increasing the polymer concentration for both PCL and PLA resulted in a slight increase in crystallinity. The PCL/PLA blend showed a slight decrease in crystallinity of the PCL phase, but the PLA phase increases in crystallinity considerably. This observation is similar to a previous study by Carmona et al.[50] as the PLA limits the mobility of PCL chains, whereas PCL provides additional mobility to the PLA chains.

Crystallinity has a significant impact on the mechanical, degradation, and biological properties of thermoplastics. Increasing crystallinity tends to improve stiffness and tensile strength, whereas the amorphous phase absorbs more impact energy.[51] During degradation of polymers, the amorphous phase is preferentially degraded.[52,53] Subsequently, polymer crystallinity is essential in tuning material properties for specific tissue engineering applications.

3.4. Tensile properties of microgroove films

The mechanical properties of the microgroove film with different topographical designs, thickness (10, 20, and 30 µm), and concentrations (1, 3, and 5 wt%) were assessed using tensile testing (Figure 5). The PCL films had a significantly higher tensile strength (~18.1 MPa) and maximum strain (~4.3 mm/mm) in comparison to the PCL/PLA films (~12.4 MPa, ~0.15 mm/mm). The PCL/PLA films had a higher Young's modulus (~109.6 MPa) than the PCL films (~56.7 MPa), indicating the increased stiffness and deformation-resistant properties of PCL/PLA
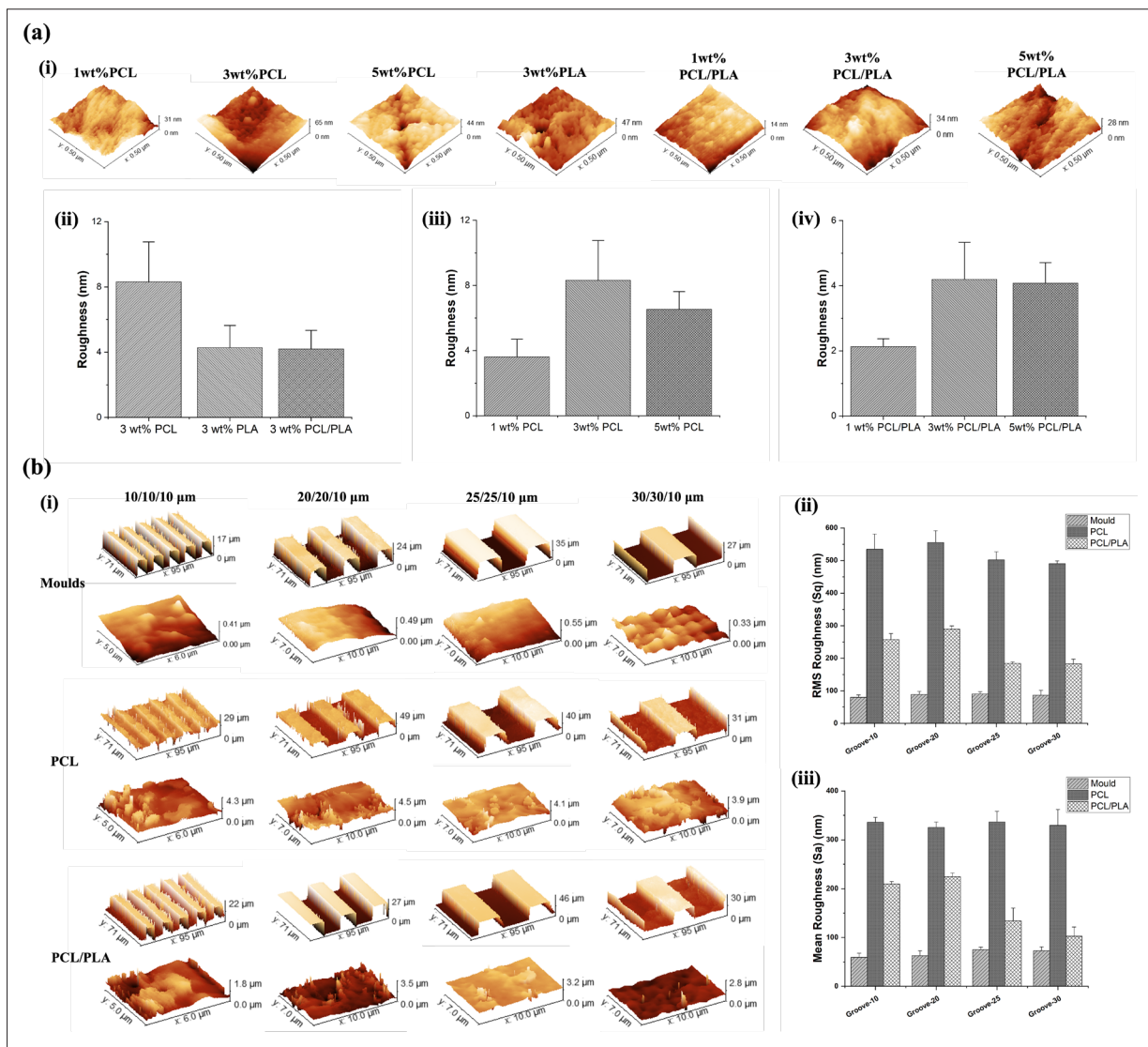
Figure 3. (a) AFM results of flat PCL, PLA, and PCL/PLA thin films with different concentration. (i) Images of the films and roughness comparison among (ii) the PCL, PLA, and PCL/PLA thin films (3 wt% concentration), (iii) different concentration PCL films, and (iv) different concentration PCL/PLA films. (b) 3D LSCM results of 3D-printed master mould and 3 wt% microgroove thin films. (i) Images of the 3D-printed moulds and thin films, (ii) the RMS roughness result, and (iii) the mean roughness result.

films, an observation consistent with previous studies.[30,54] Thus, the material compositions follow a trend of maximum tensile strength and strain at breaking of PCL>PCL/PLA and Young's modulus of PCL/PLA>PCL.

No significant difference in mechanical properties was observed as a function of microgroove size with the same film thickness. The total mass of the film is the same regardless of microgroove dimensions; therefore, any contribution by the microgroove topography to the mechanical properties is not observed or is negligible.

However, the thickness of the films had a significant influence on the mechanical properties. Among them,

the 20 µm thickness PCL groups (~17.5 MPa) showed the highest tensile strength followed by the 30 µm PCL groups (~16.5 MPa). Whilst the 10 µm thickness PCL group yielded the highest strain value (~4.04 mm/mm), smaller thickness resulted in high elongation or stretching.

The effect of different polymer concentrations (1, 3, and 5 wt%) used during solvent casting on the mechanical properties was observed using the 10 µm thickness films (Figure 5b). The mechanical properties for material composition follow a similar trend.

PCL-10 samples have a higher tensile strength and maximum strain at breaking, and lower Young's modulus
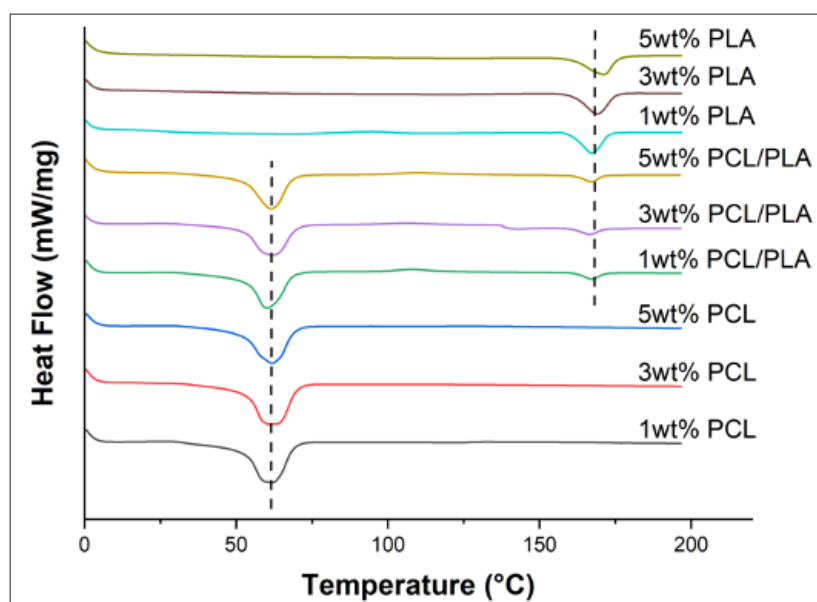
Figure 4. Thermal analysis showing DSC (1, 3, and 5 wt%) curves of PCL, PLA, and PCL/PLA blends (dotted lines represent the T_m).

Table 2. Thermal data for PCL, PLA, and PCL/PLA blend with 1, 3, and 5 wt% concentration.

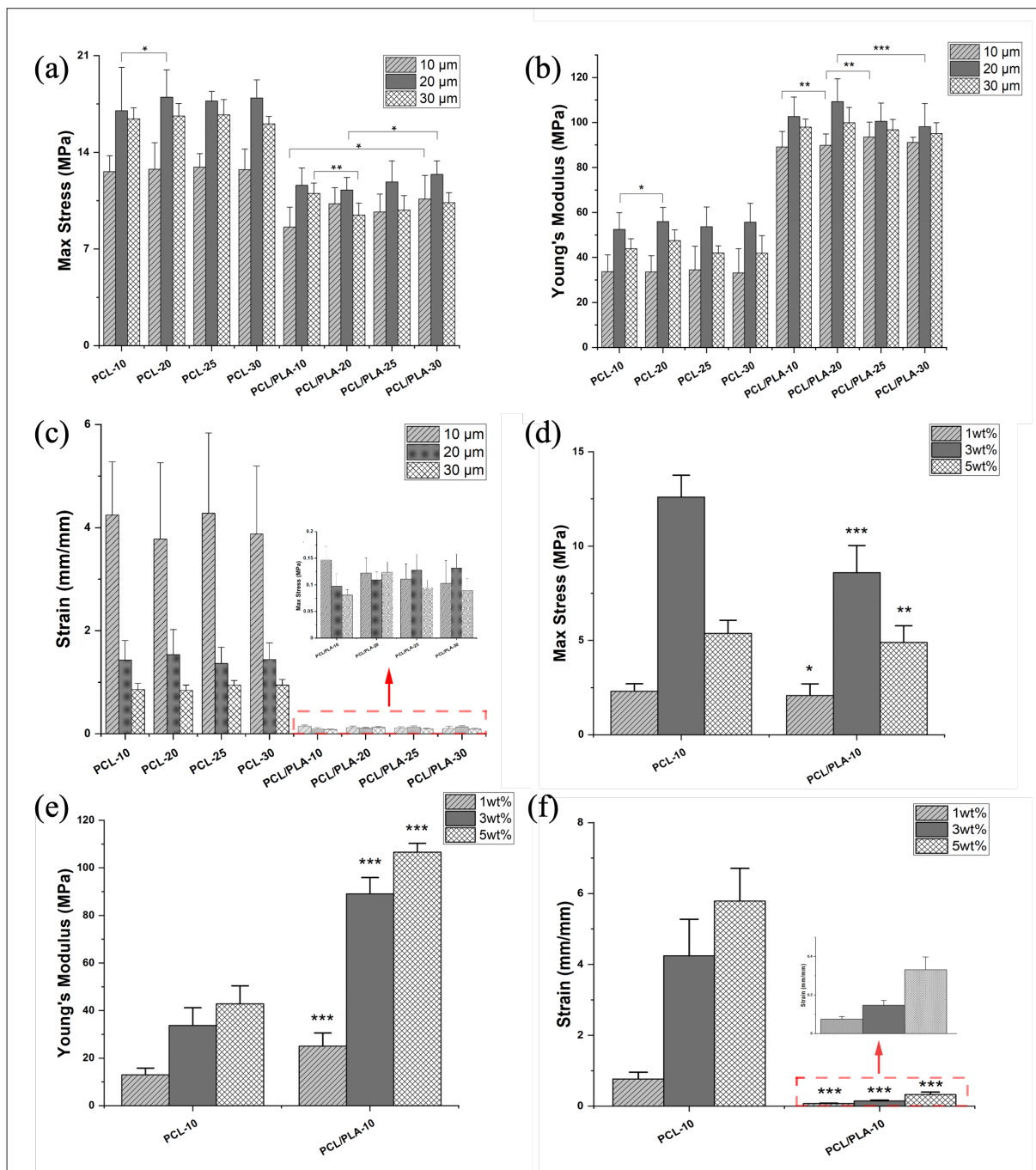|	wt%	PCL			PLA		
		T_m (°C)	ΔH_m (J/g)	X_c (%)	T_m (°C)	ΔH_m (J/g)	X_c (%)
PCL	1	62.51	68.80	52.12	/	/	/
	3	62.34	77.40	58.63	/	/	/
	5	61.97	71.49	54.16	/	/	/
PLA	1	/	/	/	167.59	23.31	24.88
	3	/	/	/	168.88	24.33	25.97
	5	/	/	/	170.61	25.15	26.84
PCL/PLA	1	61.81	54.11	51.24	166.44	5.86	31.27
	3	61.72	60.52	57.31	166.79	6.12	32.65
	5	60.25	56.30	53.31	167.37	6.15	32.82

compared to PCL/PLA-10. The 3 wt% PCL-10 and PCL/PLA-10 films had higher tensile strength (12.60 MPa and 8.59 MPa, respectively) than 1 and 5 wt% PCL-10 and PCL/PLA-10. However, the 5 wt% samples had the highest Young's modulus and maximum strain. The 1 wt% samples showed the lowest maximum stress, Young's modulus, and maximum strain. The concentration of the polymer solution, the polymer molecular weight, and the nucleating agents all influence the crystal microstructure of the polymer.[52,55] The higher crystallinity of PCL films specifically and the 3 and 5 wt% PCL and PCL/PLA films can contribute to the improved mechanical properties observed.

Further investigation is required to understand the flexural rigidity and strength of the films with the mechanical testing extended to the rolled and sealed microgroove film tubes. The current microgroove films (except 3 wt% PCL films) are within the range of reported value for maximum tensile strength of the rat sciatic nerve (1.7–7.6 MPa) and the rabbit tibial nerve (11.7 ± 0.7 MPa).[56,57] However, the Young's modulus exceeds the range of values observed in humans, rats, and rabbits.[56-58] Subsequently, the composition and design require re-evaluation. For the current study, the 3 wt% PCL/PLA samples with 10, 20, and 30 μm thickness films have the most appropriate properties for an NGC and further testing.

3.5. Surface wettability

The wettability of the microgroove surfaces (hydrophilic < 90° and hydrophobic > 90°) was evaluated to understand the role of microgroove topography, material composition, and concentration (Figure 6). The wettability can influence

Figure 5. (a) Mechanical properties of 3 wt% PCL and PCL/PLA films with different thickness showing (i) maximum tensile stress, (ii) Young's modulus, and (iii) strain at breaking. (b) Mechanical properties of 20 μm thickness film with different polymer concentration of PCL-10 and PCL/PLA-10 showing (i) maximum tensile stress, (ii) Young's modulus, and (iii) strain at breaking.

cell attachment and proliferation and requires engineering for specific applications.[59]

The films showed a significant decrease in water contact angle (WCA) from 0 to 60 s in all groups. The addition of PLA slightly reduced the WCA; hence, PCL/PLA films became more hydrophilic than PCL films. This may be related to the higher surface roughness of PCL films, the decrease in surface roughness with the inclusion of PLA in the films (Figure 3a), and the inherently less hydrophobic nature of PLA.[60] Additionally, the WCA showed a decreasing trend with increasing microgroove size. The flat samples had the
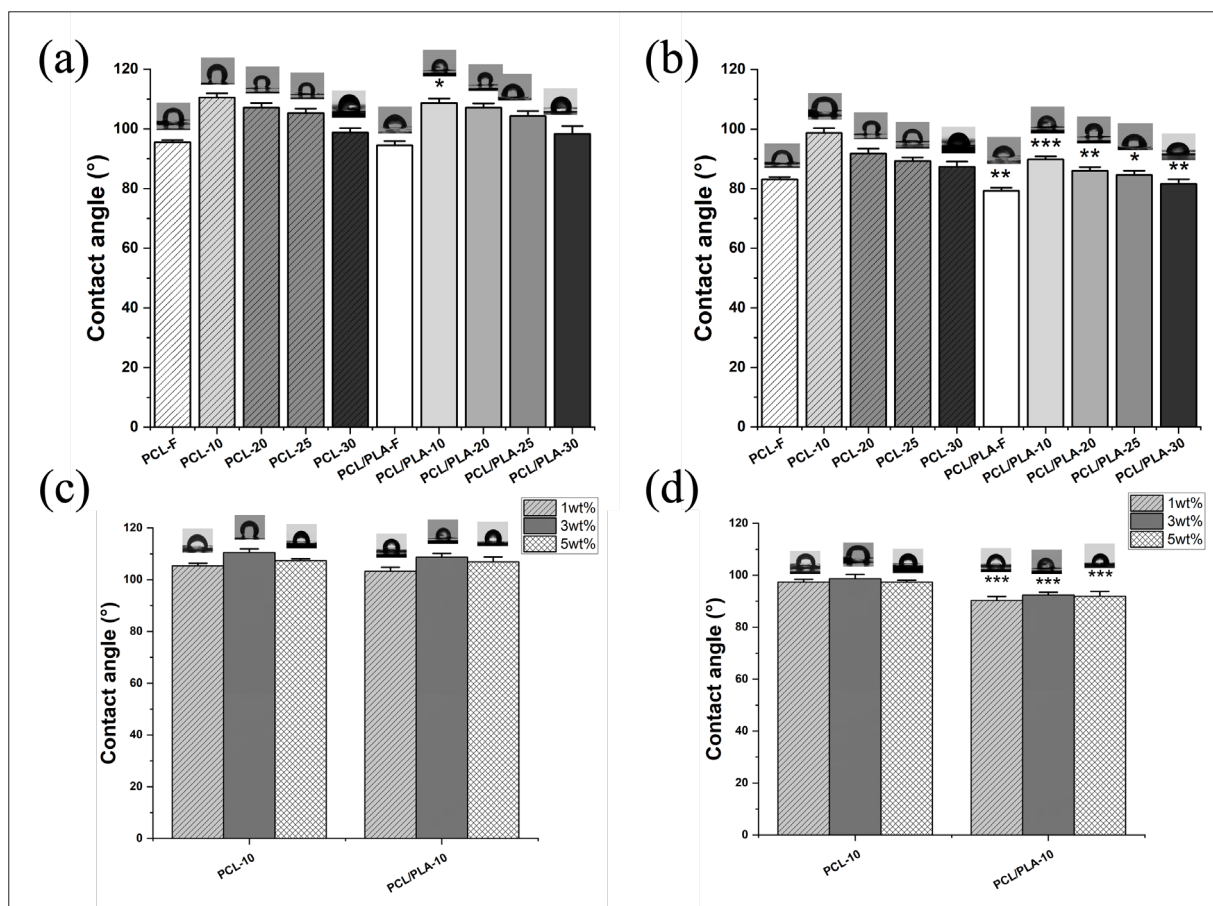
Figure 6. WCA results at (a) 0 s and (b) 60 s with different microgroove dimensions at 3 wt% concentration and for PCL-10 and PCL/PLA-10 with 1, 3, and 5 wt% concentration at (c) 0 s and (d) 60 s. *$P < 0.05$, **$P < 0.01$, and ***$P < 0.001$ between a PCL/PLA group and its corresponding PCL group.

lowest WCA. PCL-10 and PCL/PLA-10 were selected to evaluate the influence of polymer concentration (1, 3, and 5 wt%) on wettability. The 3 wt% PCL-10 and PCL/PLA-10 groups showed slightly higher WCA when compared to the 1 and 5 wt% groups, potentially due to the higher surface roughness.

3.6. Cell viability, proliferation, and alignment
The behaviour of the SH-SY5Y cells on the microgroove films was observed through cell viability, proliferation, and morphological assessment. These studies were used to determine the suitability of the PµSL 3D printing process to fabricate microgroove topographies with comparable biological properties (e.g., cell contact guidance) to conventionally fabricated microgroove films.

Cell viability was assessed on day 7 (Figure 7a and b). SH-SY5Y cells were evenly distributed on the thin film and showed high cell viability (~80%). There was no significant difference in cell viability between the material groups or

different microgroove parameters, indicating that all thin films have good cytocompatibility.

The metabolic activity of the SH-SY5Y cells was assessed through the Alamar blue assay, and the value was normalised to day 1 (Figure 7c). All samples presented a significant increase in cell metabolic activity over 7 days. Cell proliferation on flat surfaces was significantly lower than microgroove films on day 7. PCL/PLA samples showed a trend of higher proliferation than PCL. On days 3, 5, and 7 after cell seeding, the PCL-30 and PCL/PLA-30 groups showed the lowest fluorescence compared to other microgrooved groups with the same material.

The results demonstrated that microgrooves could promote cell proliferation over time compared with the flat groups, with no significant differences between microgroove groups with the same material, and that the PCL/PLA films have slightly higher cell proliferation than PCL films.

Evaluation of cell morphology on day 7 revealed that the material composition and microgroove topography
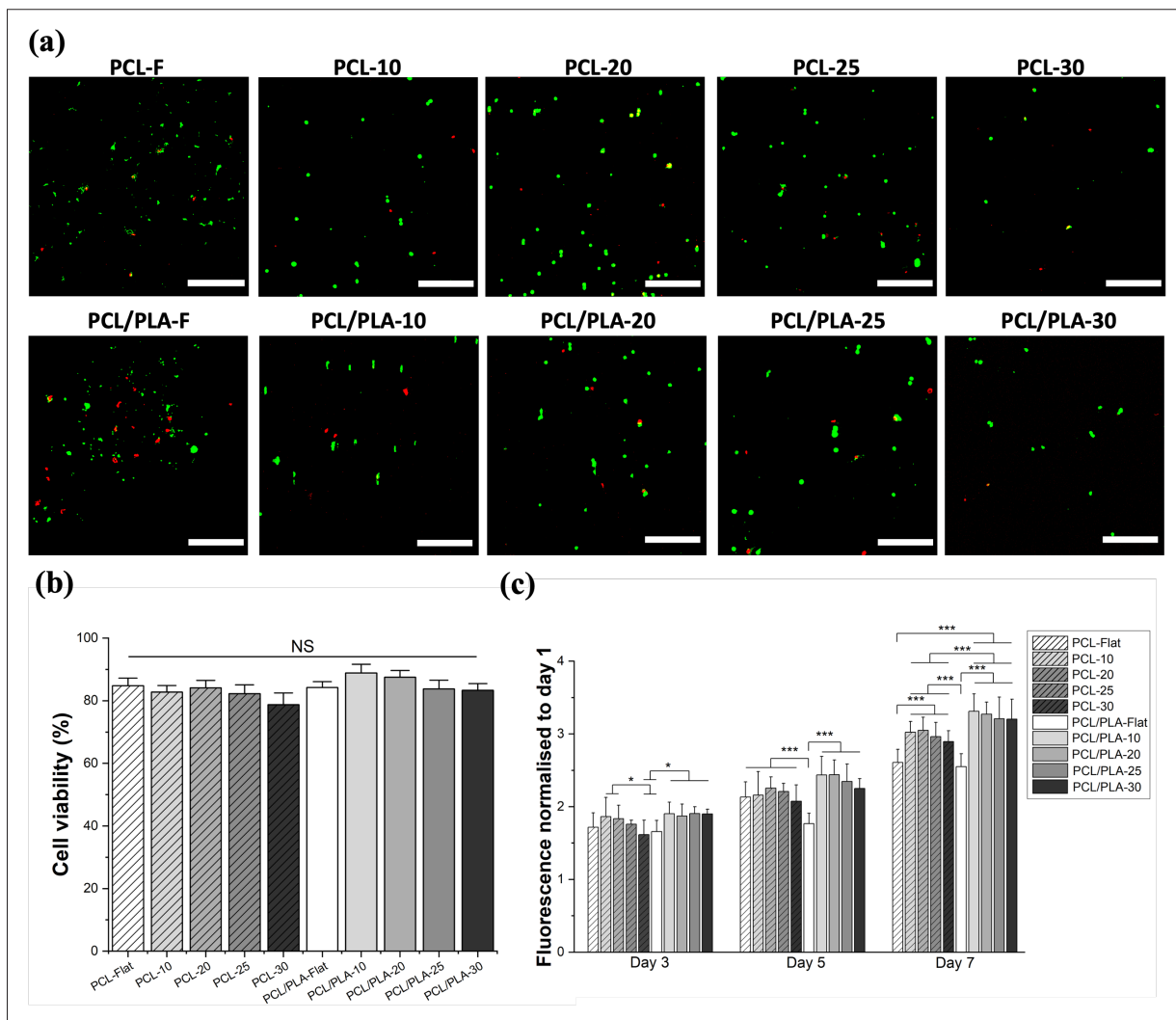
Figure 7. (a) Confocal microscopic images showing live (green) and dead (red) cells on day 7 (scale bar: 300 μm); (b) cell viability on day 7; (c) metabolic activity on PCL and PCL/PLA films for 7 days.

affected cell attachment, alignment, and neurite extension (Figure 8). Cells cultured on flat surfaces with no microgrooves had a spread morphology with protrusions and growth in multiple directions (Figure 8a and b). In contrast, the microgroove films induced cell alignment and confined growth in the direction of the grooves. Cells were observed typically attaching and growing within the depth of the microgroove rather than on top. Typically, only a single cell attached across the groove spacing in 10/10/10 μm and 20/20/10 μm microgrooves, but multiple cells or clusters were more regularly observed within the larger grooves.

Cell alignment was highest in the 10/10/10 μm, 20/20/10 μm, and 25/25/10 μm microgroove groups with an orientation angle close to 0° (Figure 9a and b). Cells

cultured on PCL and PCL/PLA films possessed a length of ~200 μm and ~275 μm, respectively. The cell elongation percentage and length/width ratio were significantly higher on microgrooved and PCL/PLA films compared to flat and PCL films, respectively (Figure 9c and d). The largest microgroove size (30/30/10 μm) showed the lowest cell length and elongation.

Finally, a greater number of cells were attached on the PCL/PLA microgroove films compared to those on the PCL films, consistent with the trend shown in cell proliferation. The results showed that, in addition to the influence of the material itself, the groove dimension is an important factor affecting cell attachment and morphology.

Cells can align along the microgrooves due to the topographical pattern, providing guided cytoplasmic stress
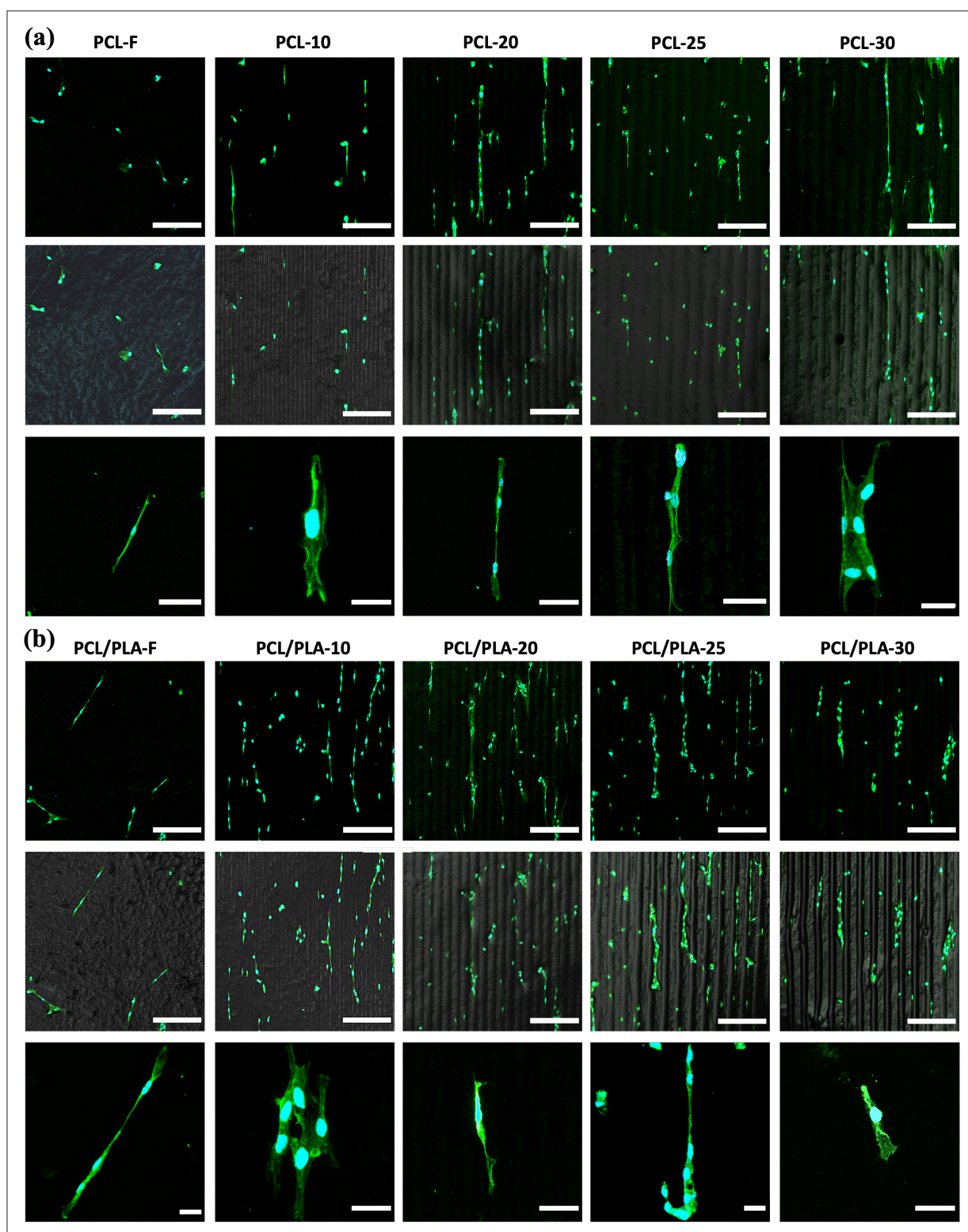
Figure 8. Confocal microscopy images of SH-SY5Y cells on (a) PCL and (b) PCL/PLA films on day 7. Cell nuclei and actin cytoskeletons, which were stained blue and green (top row), respectively, were merged with confocal reflectance (middle row) (scale bar: 200 μm), and higher-magnification images of elongated and clusters of SH-SY5Y cells (bottom row) (scale bar: 30 μm) are also shown.
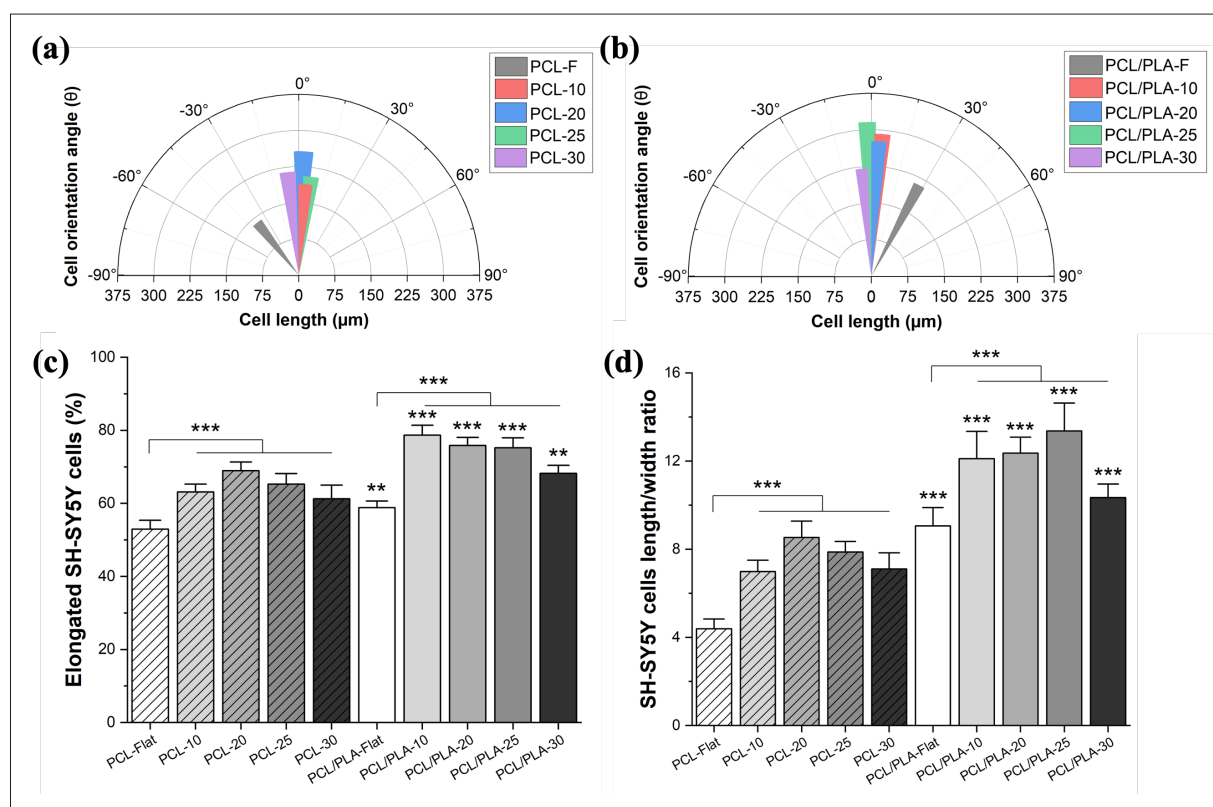
Figure 9. (a) Orientation angle of elongated SH-SY5Y cells on PCL thin films; (b) orientation angle of elongated SH-SY5Y cells on PCL/PLA thin films; (c) percentage of elongated SH-SY5Y cells; and (d) the length/width ratio of elongated SH-SY5Y cells on thin films.

to the cells, initiating multiple cellular events, and providing contact guidance.[20,21] The contact guidance can regulate cell adhesion, proliferation, differentiation, morphology, and migration. The proliferation and directional growth of cells on the PµSL-casted microgroove films observed in this study is consistent with other studies, and microgrooved NGCs were demonstrated to have higher performance compared to unpatterned NGCs.[9,27,31-33]

This study demonstrates that microgroove dimensions between 10 and 25 µm are preferable for promoting SH-SY5Y proliferation and alignment. Additionally, PCL/PLA films show higher cell proliferation potentially due to the more hydrophilic and smoother surface. The largest microgroove width, 30 µm, has a relatively lower proliferation and cell elongation, although not significant, and a large number of cell clusters. This is possibly due to the size of the smaller grooves being closer to the size of the SH-SY5Y cell body (~12 µm); therefore, cells tend to be restricted within the grooves, and axonal outgrowth is directed along the grooves, limiting axonal branching.

The observations made in this study agree with several studies.[24,29,34-36] For example, Sun et al.[24] demonstrated alignment of NG108-15 cells on microgroove films with

higher attachment and proliferation on PCL/PLA films than PCL. Mobasseri et al.[29] showed that adipose-derived stem cells (ASCs), differentiated toward a Schwann cell phenotype, preferentially aligned along ~20 µm wide microgrooves in PCL/PLA films, and that proliferation declined in flat films. Pardo-Figuerez et al.[34] showed that, in chemical patterning of cell-repulsive polymers to fabricate varying gap sizes, smaller patterns (20 µm) promoted SH-SY5Y attachment and neurite extension, as compared to larger patterns (50, 75, and 100 µm). A similar phenomenon for neurite alignment and elongation was observed by Nam et al.[35] Klein et al.[36] investigated small microgrooves (5, 8, 10, and 20 µm) and found that single SH-SY5Y cells could elongate in 5, 8, and 10 µm microgrooves, but double lines of elongated cells appeared in 20 µm microgrooves. Additionally, studies by Miller et al.[23,38] have indicated that microgrooves with a width interval of 10–20 µm are the ideal size for Schwann cell attachment and alignment.

The films investigated in this study were not treated chemically or with bioadhesion molecules, and the only engineered guidance cues were the microgroove topography. Thus, further studies are warranted to develop

advanced composite materials that include natural polymers such as gelatin, collagen, fibrin, chitosan, and silk fibroin to promote cell attachment and proliferation.[61] Furthermore, incorporation of other guidance modalities (e.g., aligned fibres and channels) and patterning of neurotrophic factors including nerve growth factor (NGF), neurotrophin-3 (NT-3), glial-derived neurotrophic factor (GDNF), and vascular endothelial growth factor (VEGF) to promote axonal outgrowth and cell migration are desirable. Additionally, the role of microgroove size and shape in other relevant neuronal cell types should be explored. The versatility of the PµSL casting technique enables these further outlined studies to be achieved.

4. Conclusion

This study used PµSL 3D printing as an alternative to the expensive, time-consuming, and complex conventional photolithography techniques to fabricate master moulds for the casting of microgroove topographies for PNI applications. The 3D-printed master moulds and the casted PDMS moulds closely match the microgroove design and exhibit high-quality surface features. This enabled the casting of biodegradable PCL and PCL/PLA films with microgroove topographies (10/10/10, 20/20/10, 25/25/10, and 30/30/10 µm) that could be assembled into a cylindrical NGC.

The PCL/PLA films exhibited a more hydrophilic and smoother surface with lower mechanical properties, closer to native peripheral nerve tissue, in comparison to PCL. PCL and PCL/PLA showed high SH-SY5Y cell viability, but higher cell attachment and proliferation was observed on PCL/PLA films. All microgroove films induced cell alignment. The smaller microgrooves (10–25 µm) exhibited a more highly ordered cell arrangement and elongation with less cell clustering. Thus, the PCL/PLA smaller microgroove films show potential for inducing cell contact guidance for peripheral nerve applications.

The simplicity and low cost of the PµSL approach to fabricate the master mould offer the potential to directly cast samples and remove the intermediate PDMS mould. This can help accelerate the manufacturing process, and extra moulds can be printed rapidly in the case of master mould damage. Furthermore, 3D printing can allow the development of more complex moulds to fabricate the entire cylindrical conduit whilst incorporating microgroove topographies. This is especially relevant for non-photocrosslinkable biomaterials, as demonstrated in this study, that are not suitable for direct processing with PµSL. Subsequently, this study establishes the potential of using PµSL for fabricating microtemplated moulds for PNI applications.

Conflict of interest

The authors declare no conflicts of interest.

Author contributions

Conceptualization: Hexin Yue, Cian Vyas, Paulo Bartolo
Formal analysis: Hexin Yue, Cian Vyas
Investigation: Hexin Yue, Xuzhao Liu, Kejian Hou, Cian Vyas
Methodology: Hexin Yue, Xuzhao Liu, Kejian Hou, Cian Vyas
Writing – original draft: Hexin Yue
Writing – review & editing: Cian Vyas, Paulo Bartolo

Ethics approval and consent to participate

Not applicable.

Consent for publication

Not applicable.

Availability of data

The data utilised in this study are available from the corresponding author upon reasonable request.

References

1. Lackington WA, Ryan AJ, O'Brien FJ. Advances in nerve guidance conduit-based therapeutics for peripheral nerve repair. *ACS Biomater Sci Eng.* 2017;3(7):1221-1235.
   doi: 10.1021/acsbiomaterials.6b00500

2. Bryan DJ, Tang JB, Doherty SA, et al. Enhanced peripheral nerve regeneration through a poled bioresorbable poly (lactic-co-glycolic acid) guidance channel. *J Neural Eng.* 2004;1(2):91.
   doi: 10.1088/1741-2560/1/2/004

3. Slavin BR, Sarhane KA, von Guionneau N, et al. Insulin-like growth factor-1: a promising therapeutic target for peripheral nerve injury. *Front Bioeng Biotechnol.* 2021;9:695850.
   doi: 10.3389/fbioe.2021.695850

4. Pabari A, Yang SY, Seifalian AM, Mosahebi A. Modern surgical management of peripheral nerve gap. *J Plast Reconstr Aesthet Surg*. 2010;63(12):1941-1948.
doi: 10.1016/j.bjps.2009.12.010

5. Vijayavenkataraman S. Nerve guide conduits for peripheral nerve injury repair: a review on design, materials and fabrication methods. *Acta Biomater*. 2020;106:54-69.
doi: 10.1016/j.actbio.2020.02.003

6. Wang ML, Rivlin M, Graham JG, Beredjiklian PK. Peripheral nerve injury, scarring, and recovery. *Connect Tissue Res*. 2019;60(1):3-9.
doi: 10.1080/03008207.2018.1489381

7. Siemionow M, Brzezicki G. Chapter 8: Current techniques and concepts in peripheral nerve repair. *Int Rev Neurobiol*. 2009;87:141-172.
doi: 10.1016/S0074-7742(09)87008-6

8. Deumens R, Bozkurt A, Meek MF, et al. Repairing injured peripheral nerves: bridging the gap. *Prog Neurobiol*. 2010;92(3):245-276.
doi: 10.1016/j.pneurobio.2010.10.002

9. Suo H, Wang Z, Dai G, Fu J, Yin J, Chang L. Polyacrylonitrile nerve conduits with inner longitudinal grooved textures to enhance neuron directional outgrowth. *J Microelectromech Syst*. 2018;27(3):457-463.
doi: 10.1109/JMEMS.2018.2810097

10. Taylor CS, Haycock JW. Biomaterials and scaffolds for repair of the peripheral nervous system. In: Phillips JB, Hercher D, Hausner T, eds. *Peripheral Nerve Tissue Engineering and Regeneration*. Cham: Springer; 2022: 245-279.
doi: 10.1007/978-3-030-21052-6_3

11. Wangensteen KJ, Kalliainen LK. Collagen tube conduits in peripheral nerve repair: a retrospective analysis. *Hand*. 2010;5(3):273-277.
doi: 10.1007/s11552-009-9245-0

12. Spivey EC, Khaing ZZ, Shear JB, Schmidt CE. The fundamental role of subcellular topography in peripheral nerve repair therapies. *Biomaterials*. 2012;33(17): 4264-4276.
doi: 10.1016/j.biomaterials.2012.02.043

13. Kehoe S, Zhang XF, Boyd D. FDA approved guidance conduits and wraps for peripheral nerve injury: a review of materials and efficacy. *Injury*. 2012;43(5):553-572.
doi: 10.1016/j.injury.2010.12.030

14. Papadimitriou L, Manganas P, Ranella A, Stratakis E. Biofabrication for neural tissue engineering applications. *Mater Today Bio*. 2020;6:100043.
doi: 10.1016/j.mtbio.2020.100043

15. Tonda-Turo C, Gnavi S, Ruini F, et al. Development and characterization of novel agar and gelatin injectable hydrogel as filler for peripheral nerve guidance channels. *J Tissue Eng Regen Med*. 2017;11(1):197-208.
doi: 10.1002/term.1902

16. Du J, Liu J, Yao S, et al. Prompt peripheral nerve regeneration induced by a hierarchically aligned fibrin nanofiber hydrogel. *Acta Biomater*. 2017;55:296-309.
doi: 10.1016/j.actbio.2017.04.010

17. Ma Y, Wang H, Wang Q, Cao X, Gao H. Piezoelectric conduit combined with multi-channel conductive scaffold for peripheral nerve regeneration. *Chem Eng J*. 2023;452: 139424.
doi: 10.1016/j.cej.2022.139424

18. Sharma AD, Zbarska S, Petersen EM, Marti ME, Mallapragada SK, Sakaguchi DS. Oriented growth and transdifferentiation of mesenchymal stem cells towards a Schwann cell fate on micropatterned substrates. *J Biosci Bioeng*. 2016;121(3):325-335.
doi: 10.1016/j.jbiosc.2015.07.006

19. Long Y, Zhang N, Huang Y, Wen X. Formation of highly aligned grooves on inner surface of semipermeable hollow fiber membrane for directional axonal outgrowth. *J Manuf Sci Eng*. 2008;130(2):021011.
doi: 10.1115/1.2896111

20. Yang CY, Huang WY, Chen LH, et al. Neural tissue engineering: the influence of scaffold surface topography and extracellular matrix microenvironment. *J Mater Chem B*. 2021;9(3):567-584.
doi: 10.1039/d0tb01605e

21. Ma Y, Gao H, Wang H, Cao X. Engineering topography: effects on nerve cell behaviors and applications in peripheral nerve repair. *J Mater Chem B*. 2021;9(32):6310-6325.
doi: 10.1039/d1tb00782c

22. Zhang D, Wu S, Feng J, Duan Y, Xing D, Gao C. Micropatterned biodegradable polyesters clicked with CQAASIKVAV promote cell alignment, directional migration, and neurite outgrowth. *Acta Biomater*. 2018;74:143-155.
doi: 10.1016/j.actbio.2018.05.018

23. Miller C, Jeftinija S, Mallapragada S. Micropatterned Schwann cell-seeded biodegradable polymer substrates significantly enhance neurite alignment and outgrowth. *Tissue Eng*. 2001;7(6):705-715.
doi: 10.1089/107632701753337663

24. Sun M, Kingham PJ, Reid AJ, Armstrong SJ, Terenghi G, Downes S. In vitro and in vivo testing of novel ultrathin PCL and PCL/PLA blend films as peripheral nerve conduit. *J Biomed Mater Res Part A*. 2010;93(4):1470-1481.
doi: 10.1002/jbm.a.32681

25. Hwang CM, Park Y, Park JY, et al. Controlled cellular orientation on PLGA microfibers with defined diameters. *Biomed Microdevices*. 2009;11(4):739-746.
doi: 10.1007/s10544-009-9287-7

26. Hsu SH, Lu PS, Ni HC, Su CH. Fabrication and evaluation of microgrooved polymers as peripheral nerve conduits. *Biomed Microdevices*. 2007;9:665-674.
doi: 10.1007/s10544-007-9068-0

27. Béduer A, Vieu C, Arnauduc F, Sol JC, Loubinoux I, Vaysse L. Engineering of adult human neural stem cells differentiation through surface micropatterning. *Biomaterials*. 2012;33(2):504-514.
doi: 10.1016/j.biomaterials.2011.09.073

28. Lu S, Chen W, Wang J, et al. Polydopamine-decorated PLCL conduit to induce synergetic effect of electrical stimulation and topological morphology for peripheral nerve regeneration. *Small Methods*. 2023;7(2):e2200883.
doi: 10.1002/smtd.202200883

29. Mobasseri A, Faroni A, Minogue BM, Downes S, Terenghi G, Reid AJ. Polymer scaffolds with preferential parallel grooves enhance nerve regeneration. *Tissue Eng Part A*. 2015;21(5-6):1152-1162.
doi: 10.1089/ten.TEA.2014.0266

30. Mobasseri SA, Terenghi G, Downes S. Micro-structural geometry of thin films intended for the inner lumen of nerve conduits affects nerve repair. *J Mater Sci Mater Med*. 2013;24(7):1639-1647.
doi: 10.1007/s10856-013-4922-5

31. Hsu SH, Ni HC. Fabrication of the microgrooved/microporous polylactide substrates as peripheral nerve conduits and in vivo evaluation. *Tissue Eng Part A*. 2009;15(6):1381-1390.
doi: 10.1089/ten.tea.2008.0175

32. Litowczenko J, Maciejewska BM, Wychowaniec JK, Koscinski M, Jurga S, Warowicka A. Groove-patterned surfaces induce morphological changes in cells of neuronal origin. *J Biomed Mater Res A*. 2019;107(10):2244-2256.
doi: 10.1002/jbm.a.36733

33. Yu S, Liu D, Wang T, Lee YZ, Wong JCN, Song X. Micropatterning of polymer substrates for cell culture. *J Biomed Mater Res B Appl Biomater*. 2021;109(10):1525-1533.
doi: 10.1002/jbm.b.34811

34. Pardo-Figuerez M, Martin NRW, Player DJ, et al. Controlled arrangement of neuronal cells on surfaces functionalized with micropatterned polymer brushes. *ACS Omega*. 2018;3(10):12383-12391.
doi: 10.1021/acsomega.8b01698

35. Nam KH, Jamilpour N, Mfoumou E, Wang FY, Zhang DD, Wong PK. Probing mechanoregulation of neuronal differentiation by plasma lithography patterned elastomeric substrates. *Sci Rep*. 2014;4(1):6965.
doi: 10.1038/srep06965

36. Klein CL, Scholl M, Maelicke A. Neuronal networks in vitro: formation and organization on biofunctionalized surfaces. *J Mater Sci Mater Med*. 1999;10(12):721-727.
doi: 10.1023/a:1008975105243

37. Qin D, Xia Y, Whitesides GM. Soft lithography for micro- and nanoscale patterning. *Nat Protoc*. 2010;5(3):491-502.
doi: 10.1038/nprot.2009.234

38. Miller C, Shanks H, Witt A, Rutkowski G, Mallapragada S. Oriented Schwann cell growth on micropatterned biodegradable polymer substrates. *Biomaterials*. 2001;22(11):1263-1269.
doi: 10.1016/s0142-9612(00)00278-7

39. Ge Q, Li Z, Wang Z, et al. Projection micro stereolithography based 3D printing and its applications. *Int J Extreme Manuf*. 2020;2(2):022004.
doi: 10.1088/2631-7990/ab8d9a

40. Evangelista MS, Perez M, Salibian AA, et al. Single-lumen and multi-lumen poly(ethylene glycol) nerve conduits fabricated by stereolithography for peripheral nerve regeneration in vivo. *J Reconstr Microsurg*. 2015;31(5):327-335.
doi: 10.1055/s-0034-1395415

41. Singh A, Asikainen S, Teotia AK, et al. Biomimetic photocurable three-dimensional printed nerve guidance channels with aligned cryomatrix lumen for peripheral nerve regeneration. *ACS Appl Mater Interfaces*. 2018;10(50):43327-43342.
doi: 10.1021/acsami.8b11677

42. Pateman CJ, Harding AJ, Glen A, et al. Nerve guides manufactured from photocurable polymers to aid peripheral nerve repair. *Biomaterials*. 2015;49:77-89.
doi: 10.1016/j.biomaterials.2015.01.055

43. Moreno-Rivas O, Hernández-Velázquez D, Piazza V, Marquez S. Rapid prototyping of microfluidic devices by SL 3D printing and their biocompatibility study for cell culturing. *Mater Today Proc*. 2019;13:436-445.
doi: 10.1016/j.matpr.2019.03.189

44. Villegas M, Cetinic Z, Shakeri A, Didar TF. Fabricating smooth PDMS microfluidic channels from low-resolution 3D printed molds using an omniphobic lubricant-infused coating. *Anal Chim Acta*. 2018;1000:248-255.
doi: 10.1016/j.aca.2017.11.063

45. Jonathan Tjong AGT, John PF. Solvent extraction of 3D printed molds for soft lithography. *R Soc Chem*. 2020.

46. Schneider CA, Rasband WS, Eliceiri KW. NIH image to ImageJ: 25 years of image analysis. *Nat Methods*. 2012;9(7):671-675.
doi: 10.1038/nmeth.2089

47. Vertuccio L, Gorrasi G, Sorrentino A, Vittoria V. Nano clay reinforced PCL/starch blends obtained by high energy ball milling. *Carbohydr Polym*. 2009;75(1):172-179.
doi: 10.1016/j.carbpol.2008.07.020

48. Tonazzini I, Cecchini A, Elgersma Y, Cecchini M. Interaction of SH-SY5Y cells with nanogratings during neuronal differentiation: comparison with primary neurons. *Adv Healthc Mater*. 2014;3(4):581-587.
doi: 10.1002/adhm.201300216

49. Alvim Valente C, Cesar Chagastelles P, Fontana Nicoletti N, et al. Design and optimization of biocompatible

polycaprolactone/poly (l-lactic-co-glycolic acid) scaffolds with and without microgrooves for tissue engineering applications. *J Biomed Mater Res Part A*. 2018;106(6): 1522-1534.
doi: 10.1002/jbm.a.36355

50. Carmona VB, Corrêa AC, Marconcini JM, Mattoso LHC. Properties of a biodegradable ternary blend of thermoplastic starch (TPS), poly (ε-caprolactone)(PCL) and poly (lactic acid)(PLA). *J Polym Environ*. 2015;23(1): 83-89.
doi: 10.1007/s10924-014-0666-7

51. Vieille B, Albouy W, Chevalier L, Taleb L. About the influence of stamping on thermoplastic-based composites for aeronautical applications. *Compos Part B: Eng*. 2013;45(1):821-834.
doi: 10.1016/j.compositesb.2012.07.047

52. Kostakova E, Mészáros L, Maskova G, Blazkova L, Turcsan T, Lukas D. Crystallinity of electrospun and centrifugal spun polycaprolactone fibers: a comparative study. *J Nanomater*. 2017;1-9.
doi: 10.1155/2017/8952390

53. Huang B, Wang Y, Vyas C, Bartolo P. Crystal growth of 3D poly(ε-caprolactone) based bone scaffolds and its effects on the physical properties and cellular interactions. *Adv Sci*. 2023;10(1):2203183.
doi: 10.1002/advs.202203183

54. Sun M, Downes S. Physicochemical characterisation of novel ultra-thin biodegradable scaffolds for peripheral nerve repair. *J Mater Sci Mater Med*. 2009;20(5):1181-1192.
doi: 10.1007/s10856-008-3671-3

55. Dong J, Liu J, Li X, Liang Q, Xu X. Relationship between the Young's modulus and the crystallinity of cross-linked poly (ε-caprolactone) as an immobilization membrane for cancer radiotherapy. *Glob Chall*. 2020;4(8):2000008.
doi: 10.1002/gch2.202000008

56. Borschel GH, Kia KF, Kuzon WM, Jr., Dennis RG. Mechanical properties of acellular peripheral nerve. *J Surg Res*. 2003;114(2):133-139.
doi: 10.1016/s0022-4804(03)00255-5

57. Rydevik BL, Kwan MK, Myers RR, et al. An in vitro mechanical and histological study of acute stretching on rabbit tibial nerve. *J Orthop Res*. 1990;8(5):694-701.
doi: 10.1002/jor.1100080511

58. Kerns J, Piponov H, Helder C, Amirouche F, Solitro G, Gonzalez M. Mechanical properties of the human tibial and peroneal nerves following stretch with histological correlations. *Anat Rec*. 2019;302(11):2030-2039.
doi: 10.1002/ar.24250

59. Rahmati M, Silva EA, Reseland JE, Heyward CA, Haugen HJ. Biological responses to physicochemical properties of biomaterial surface. *Chem Soc Rev*. 2020;49(15):5178-5224.
doi: 10.1039/D0CS00103A

60. Patr T, Glória A. Mechanical and biological behaviour of PCL and PCL/PLA scaffolds for tissue engineering applications. *Chem Eng Trans*. 2013;32:1645-1650.
doi: 10.3303/CET1332275

61. Zhang H, Guo J, Wang Y, Shang L, Chai R, Zhao Y. Natural polymer-derived bioscaffolds for peripheral nerve regeneration. *Adv Funct Mater*. 2022;32(41):2203829.
doi: 10.1002/adfm.202203829